

Di-electron spectrum at mid-rapidity in $p + p$ collisions at $\sqrt{s} = 200$ GeV

L. Adamczyk,¹ G. Agakishiev,²⁰ M. M. Aggarwal,³¹ Z. Ahammed,⁵⁰ A. V. Alakhverdyants,²⁰ I. Alekseev,¹⁸ J. Alford,²¹ B. D. Anderson,²¹ C. D. Anson,²⁹ D. Arkhipkin,³ E. Aschenauer,³ G. S. Averichev,²⁰ J. Balewski,²⁵ A. Banerjee,⁵⁰ Z. Barnovska,¹³ D. R. Beavis,³ R. Bellwied,⁴⁶ M. J. Betancourt,²⁵ R. R. Betts,⁹ A. Bhasin,¹⁹ A. K. Bhati,³¹ H. Bichsel,⁵² J. Bielcik,¹² J. Bielcikova,¹³ L. C. Bland,³ I. G. Bordyuzhin,¹⁸ W. Borowski,⁴³ J. Bouchet,²¹ A. V. Brandin,²⁸ S. G. Brovko,⁵ E. Bruna,⁵⁴ S. Bueltmann,³⁰ I. Bunzarov,²⁰ T. P. Burton,³ J. Butterworth,³⁸ X. Z. Cai,⁴² H. Caines,⁵⁴ M. Calderón de la Barca Sánchez,⁵ D. Cebra,⁵ R. Cendejas,⁶ M. C. Cervantes,⁴⁴ P. Chaloupka,¹³ Z. Chang,⁴⁴ S. Chattopadhyay,⁵⁰ H. F. Chen,⁴⁰ J. H. Chen,⁴² J. Y. Chen,⁸ L. Chen,⁸ J. Cheng,⁴⁷ M. Cherney,¹¹ A. Chikanian,⁵⁴ W. Christie,³ P. Chung,¹³ J. Chwastowski,¹⁰ M. J. M. Coddington,⁴⁴ R. Corliss,²⁵ J. G. Cramer,⁵² H. J. Crawford,⁴ X. Cui,⁴⁰ A. Davila Leyva,⁴⁵ L. C. De Silva,⁴⁶ R. R. Debbé,³ T. G. Dedovich,²⁰ J. Deng,⁴¹ R. Derradi de Souza,⁷ S. Dhamija,¹⁷ L. Didenko,³ F. Ding,⁵ A. Dion,³ P. Djawotho,⁴⁴ X. Dong,²⁴ J. L. Drachenberg,⁴⁴ J. E. Draper,⁵ C. M. Du,²³ L. E. Dunkelberger,⁶ J. C. Dunlop,³ L. G. Efimov,²⁰ M. Elnimr,⁵³ J. Engelage,⁴ G. Eppley,³⁸ L. Eun,²⁴ O. Evdokimov,⁹ R. Fatemi,²² S. Fazio,³ J. Fedorisin,²⁰ R. G. Fersch,²² P. Filip,²⁰ E. Finch,⁵⁴ Y. Fisyak,³ C. A. Gagliardi,⁴⁴ D. R. Gangadharan,²⁹ F. Geurts,³⁸ A. Gibson,⁴⁹ S. Gliske,² Y. N. Gorbunov,¹¹ O. G. Grebenyuk,²⁴ D. Grosnick,⁴⁹ S. Gupta,¹⁹ W. Guryn,³ B. Haag,⁵ O. Hajkova,¹² A. Hamed,⁴⁴ L-X. Han,⁴² J. W. Harris,⁵⁴ J. P. Hays-Wehle,²⁵ S. Heppelmann,³³ A. Hirsch,³⁵ G. W. Hoffmann,⁴⁵ D. J. Hofman,⁹ S. Horvat,⁵⁴ B. Huang,³ H. Z. Huang,⁶ P. Huck,⁸ T. J. Humanic,²⁹ L. Huo,⁴⁴ G. Igo,⁶ W. W. Jacobs,¹⁷ C. Jena,¹⁵ J. Joseph,²¹ E. G. Judd,⁴ S. Kabana,⁴³ K. Kang,⁴⁷ J. Kapitan,¹³ K. Kauder,⁹ H. W. Ke,⁸ D. Keane,²¹ A. Kechechyan,²⁰ A. Kesich,⁵ D. Kettler,⁵² D. P. Kikola,³⁵ J. Kiryluk,²⁴ A. Kisiel,⁵¹ V. Kizka,²⁰ S. R. Klein,²⁴ D. D. Koetke,⁴⁹ T. Kollegger,¹⁴ J. Konzer,³⁵ I. Koralt,³⁰ L. Koroleva,¹⁸ W. Korsch,²² L. Kotchenda,²⁸ P. Kravtsov,²⁸ K. Krueger,² L. Kumar,²¹ M. A. C. Lamont,³ J. M. Landgraf,³ S. LaPointe,⁵³ J. Lauret,³ A. Lebedev,³ R. Lednicky,²⁰ J. H. Lee,³ W. Leight,²⁵ M. J. LeVine,³ C. Li,⁴⁰ L. Li,⁴⁵ W. Li,⁴² X. Li,³⁵ X. Li,⁴¹ Y. Li,⁴⁷ Z. M. Li,⁸ L. M. Lima,³⁹ M. A. Lisa,²⁹ F. Liu,⁸ T. Ljubicic,³ W. J. Llope,³⁸ R. S. Longacre,³ Y. Lu,⁴⁰ X. Luo,⁸ A. Luszczak,¹⁰ G. L. Ma,⁴² Y. G. Ma,⁴² D. M. M. D. Madagadagettige Don,¹¹ D. P. Mahapatra,¹⁵ R. Majka,⁵⁴ O. I. Mall,⁵ S. Margetis,²¹ C. Markert,⁴⁵ H. Masui,²⁴ H. S. Matis,²⁴ D. McDonald,³⁸ T. S. McShane,¹¹ S. Mioduszewski,⁴⁴ M. K. Mitrovski,³ Y. Mohammed,⁴⁴ B. Mohanty,⁵⁰ M. M. Mondal,⁴⁴ B. Morozov,¹⁸ M. G. Munhoz,³⁹ M. K. Mustafa,³⁵ M. Naglis,²⁴ B. K. Nandi,¹⁶ Md. Nasim,⁵⁰ T. K. Nayak,⁵⁰ L. V. Nogach,³⁴ J. Novak,²⁷ G. Odyniec,²⁴ A. Ogawa,³ K. Oh,³⁶ A. Ohlson,⁵⁴ V. Okorokov,²⁸ E. W. Oldag,⁴⁵ R. A. N. Oliveira,³⁹ D. Olson,²⁴ P. Ostrowski,⁵¹ M. Pachr,¹² B. S. Page,¹⁷ S. K. Pal,⁵⁰ Y. X. Pan,⁶ Y. Pandit,²¹ Y. Panebratsev,²⁰ T. Pawlak,⁵¹ B. Pawlik,³² H. Pei,⁹ C. Perkins,⁴ W. Peryt,⁵¹ P. Pile,³ M. Planinic,⁵⁵ J. Pluta,⁵¹ D. Plyku,³⁰ N. Poljak,⁵⁵ J. Porter,²⁴ A. M. Poskanzer,²⁴ C. B. Powell,²⁴ D. Prindle,⁵² C. Pruneau,⁵³ N. K. Pruthi,³¹ M. Przybycien,¹ P. R. Pujahari,¹⁶ J. Putschke,⁵³ H. Qiu,²⁴ R. Raniwala,³⁷ S. Raniwala,³⁷ R. L. Ray,⁴⁵ R. Redwine,²⁵ R. Reed,⁵ C. K. Riley,⁵⁴ H. G. Ritter,²⁴ J. B. Roberts,³⁸ O. V. Rogachevskiy,²⁰ J. L. Romero,⁵ J. F. Ross,¹¹ L. Ruan,³ J. Rusnak,¹³ N. R. Sahoo,⁵⁰ I. Sakrejda,²⁴ S. Salur,²⁴ A. Sandacz,⁵¹ J. Sandweiss,⁵⁴ E. Sangaline,⁵ A. Sarkar,¹⁶ J. Schambach,⁴⁵ R. P. Scharenberg,³⁵ A. M. Schmah,²⁴ B. Schmidke,³ N. Schmitz,²⁶ T. R. Schuster,¹⁴ J. Seele,²⁵ J. Seger,¹¹ P. Seyboth,²⁶ N. Shah,⁶ E. Shalaliev,²⁰ M. Shao,⁴⁰ B. Sharma,³¹ M. Sharma,⁵³ S. S. Shi,⁸ Q. Y. Shou,⁴² E. P. Sichtermann,²⁴ R. N. Singaraju,⁵⁰ M. J. Skoby,³⁵ D. Smirnov,³ N. Smirnov,⁵⁴ D. Solanki,³⁷ P. Sorensen,³ U. G. deSouza,³⁹ H. M. Spinka,² B. Srivastava,³⁵ T. D. S. Stanislaus,⁴⁹ S. G. Steadman,²⁵ J. R. Stevens,¹⁷ R. Stock,¹⁴ M. Strikhanov,²⁸ B. Stringfellow,³⁵ A. A. P. Suaide,³⁹ M. C. Suarez,⁹ M. Sumera,¹³ X. M. Sun,²⁴ Y. Sun,⁴⁰ Z. Sun,²³ B. Surov,²⁵ D. N. Svirida,¹⁸ T. J. M. Symons,²⁴ A. Szanto de Toledo,³⁹ J. Takahashi,⁷ A. H. Tang,³ Z. Tang,⁴⁰ L. H. Tarini,⁵³ T. Tarnowsky,²⁷ D. Thein,⁴⁵ J. H. Thomas,²⁴ J. Tian,⁴² A. R. Timmins,⁴⁶ D. Tlusty,¹³ M. Tokarev,²⁰ T. A. Trainor,⁵² S. Trentalange,⁶ R. E. Tribble,⁴⁴ P. Tribedy,⁵⁰ B. A. Trzeciak,⁵¹ O. D. Tsai,⁶ J. Turnau,³² T. Ullrich,³ D. G. Underwood,² G. Van Buren,³ G. van Nieuwenhuizen,²⁵ J. A. Vanfossen, Jr.,²¹ R. Varma,¹⁶ G. M. S. Vasconcelos,⁷ F. Videbæk,³ Y. P. Vijoyi,⁵⁰ S. Vokal,²⁰ S. A. Voloshin,⁵³ A. Vossen,¹⁷ M. Wada,⁴⁵ F. Wang,³⁵ G. Wang,⁶ H. Wang,²⁷ J. S. Wang,²³ Q. Wang,³⁵ X. L. Wang,⁴⁰ Y. Wang,⁴⁷ G. Webb,²² J. C. Webb,³ G. D. Westfall,²⁷ C. Whitten Jr.,⁶ H. Wieman,²⁴ S. W. Wissink,¹⁷ R. Witt,⁴⁸ W. Witzke,²² Y. F. Wu,⁸ Z. Xiao,⁴⁷ W. Xie,³⁵ K. Xin,³⁸ H. Xu,²³ N. Xu,²⁴ Q. H. Xu,⁴¹ W. Xu,⁶ Y. Xu,⁴⁰ Z. Xu,³ L. Xue,⁴² Y. Yang,²³ Y. Yang,⁸ P. Yepes,³⁸ Y. Yi,³⁵ K. Yip,³ I-K. Yoo,³⁶ M. Zawisza,⁵¹ H. Zbroszczyk,⁵¹ J. B. Zhang,⁸ S. Zhang,⁴² W. M. Zhang,²¹ X. P. Zhang,⁴⁷ Y. Zhang,⁴⁰ Z. P. Zhang,⁴⁰ F. Zhao,⁶ J. Zhao,⁴² C. Zhong,⁴² X. Zhu,⁴⁷ Y. H. Zhu,⁴² and Y. Zoulkarneeva²⁰

(STAR Collaboration)

¹AGH University of Science and Technology, Cracow, Poland

- ²Argonne National Laboratory, Argonne, Illinois 60439, USA
³Brookhaven National Laboratory, Upton, New York 11973, USA
⁴University of California, Berkeley, California 94720, USA
⁵University of California, Davis, California 95616, USA
⁶University of California, Los Angeles, California 90095, USA
⁷Universidade Estadual de Campinas, Sao Paulo, Brazil
⁸Central China Normal University (HZNU), Wuhan 430079, China
⁹University of Illinois at Chicago, Chicago, Illinois 60607, USA
¹⁰Krakov University of Technology, Crakow, Poland
¹¹Creighton University, Omaha, Nebraska 68178, USA
¹²Czech Technical University in Prague, FNSPE, Prague, 115 19, Czech Republic
¹³Nuclear Physics Institute AS CR, 250 68 Řež/Prague, Czech Republic
¹⁴University of Frankfurt, Frankfurt, Germany
¹⁵Institute of Physics, Bhubaneswar 751005, India
¹⁶Indian Institute of Technology, Mumbai, India
¹⁷Indiana University, Bloomington, Indiana 47408, USA
¹⁸Alikhanov Institute for Theoretical and Experimental Physics, Moscow, Russia
¹⁹University of Jammu, Jammu 180001, India
²⁰Joint Institute for Nuclear Research, Dubna, 141 980, Russia
²¹Kent State University, Kent, Ohio 44242, USA
²²University of Kentucky, Lexington, Kentucky, 40506-0055, USA
²³Institute of Modern Physics, Lanzhou, China
²⁴Lawrence Berkeley National Laboratory, Berkeley, California 94720, USA
²⁵Massachusetts Institute of Technology, Cambridge, MA 02139-4307, USA
²⁶Max-Planck-Institut für Physik, Munich, Germany
²⁷Michigan State University, East Lansing, Michigan 48824, USA
²⁸Moscow Engineering Physics Institute, Moscow Russia
²⁹Ohio State University, Columbus, Ohio 43210, USA
³⁰Old Dominion University, Norfolk, VA, 23529, USA
³¹Panjab University, Chandigarh 160014, India
³²Institute of Nuclear Physics PAS, Cracow, Poland
³³Pennsylvania State University, University Park, Pennsylvania 16802, USA
³⁴Institute of High Energy Physics, Protvino, Russia
³⁵Purdue University, West Lafayette, Indiana 47907, USA
³⁶Pusan National University, Pusan, Republic of Korea
³⁷University of Rajasthan, Jaipur 302004, India
³⁸Rice University, Houston, Texas 77251, USA
³⁹Universidade de Sao Paulo, Sao Paulo, Brazil
⁴⁰University of Science & Technology of China, Hefei 230026, China
⁴¹Shandong University, Jinan, Shandong 250100, China
⁴²Shanghai Institute of Applied Physics, Shanghai 201800, China
⁴³SUBATECH, Nantes, France
⁴⁴Texas A&M University, College Station, Texas 77843, USA
⁴⁵University of Texas, Austin, Texas 78712, USA
⁴⁶University of Houston, Houston, TX, 77204, USA
⁴⁷Tsinghua University, Beijing 100084, China
⁴⁸United States Naval Academy, Annapolis, MD 21402, USA
⁴⁹Valparaiso University, Valparaiso, Indiana 46383, USA
⁵⁰Variable Energy Cyclotron Centre, Kolkata 700064, India
⁵¹Warsaw University of Technology, Warsaw, Poland
⁵²University of Washington, Seattle, Washington 98195, USA
⁵³Wayne State University, Detroit, Michigan 48201, USA
⁵⁴Yale University, New Haven, Connecticut 06520, USA
⁵⁵University of Zagreb, Zagreb, HR-10002, Croatia

(Dated: June 3, 2019)

We report on mid-rapidity mass spectrum of di-electrons and cross sections of pseudoscalar and vector mesons via e^+e^- decays, from $\sqrt{s} = 200$ GeV $p+p$ collisions, measured by the large acceptance experiment STAR at RHIC. The ratio of the di-electron continuum to the combinatorial background is larger than 10% over the entire mass range. Simulations of di-electrons from light-meson decays and heavy-flavor decays (charmonium and open charm correlation) are found to describe the data. The extracted $\omega \rightarrow e^+e^-$ invariant yields are consistent with previous measurements. The mid-rapidity yields (dN/dy) of ϕ and J/ψ are extracted through their di-electron decay channels and are

consistent with the previous measurements of $\phi \rightarrow K^+K^-$ and $J/\psi \rightarrow e^+e^-$. Our results suggest a new upper limit of the branching ratio of the $\eta \rightarrow e^+e^-$ of 1.7×10^{-5} at 90% confidence level.

PACS numbers:

I. INTRODUCTION

Di-leptons are a crucial probe of the strongly interacting matter, created in ultra-relativistic heavy-ion collisions [1, 2]. Leptons are produced during the whole evolution of the created matter and can traverse the medium with minimum interactions. Therefore, different kinematics of di-lepton pairs (mass and transverse momentum ranges) can selectively probe the properties of the matter throughout the whole evolution [3, 4].

In the low-mass range ($M_{ll} < 1.1 \text{ GeV}/c^2$), vector meson in-medium properties (mass and width of the spectral function of $\rho(770)$, $\omega(782)$, and $\phi(1020)$) may be studied via di-lepton decays and may exhibit modifications related to possible chiral symmetry restoration [3, 4]. For example, at the SPS, the low-mass di-lepton enhancement in the CERES e^+e^- data requires substantial medium effects on the ρ -meson spectral function [5]. Recently, a significant excess of low-mass $\mu^+\mu^-$ pairs above the yield expected from neutral meson decays has been reported by the NA60 Collaboration [6]. This low-mass enhancement is consistent with a broadened spectral function [7] but not a dropping-mass scenario [8].

At RHIC, PHENIX experiment observed a significant enhancement in the di-electron continuum in Au+Au collisions compared to expectations from hadronic sources at $0.15 < M_{ee} < 0.75 \text{ GeV}/c^2$ at low transverse momentum ($p_T < 1 \text{ GeV}/c$) [9], while at higher p_T in the same mass region, direct photon yields were derived through di-electron measurements at RHIC for an assessment of thermal radiation [10]. The models, which describe the SPS di-lepton data, fail to consistently describe the PHENIX data in the low-mass and low- p_T region [9, 11]. Additional precision experiments with large acceptance and a broad range of beam energies can provide invaluable insights in this subject [1].

The di-lepton spectra in the intermediate mass range ($1.1 < M_{ll} < 3.0 \text{ GeV}/c^2$) are expected to be directly related to the thermal radiation of the Quark-Gluon Plasma (QGP) [3, 4]. However, significant background contributions from other sources have to be measured experimentally. Such contributions include background pairs from correlated open heavy-flavor decays, which produce a pair of electrons or muons from the semileptonic decay of a pair of open charm or bottom hadrons ($c\bar{c} \rightarrow l^+l^-$ or $b\bar{b} \rightarrow l^+l^-$). In the high-mass region ($M_{ll} > 3.0 \text{ GeV}/c^2$), J/ψ , Υ , and their excited states are used to study the color screening features of the QGP [12]. The first di-electron continuum measurement

from STAR in $\sqrt{s} = 200 \text{ GeV}$ $p+p$ collisions, presented in this paper, provides a crucial reference for corresponding future STAR measurements in heavy-ion collisions.

Rare processes like leptonic decays of hadrons provide possible observables in searching for traces of new physics Beyond the Standard Model (BSM) [13–16]. These decays usually involve electromagnetic or weak couplings which can be calculated to a high degree of accuracy within the Standard Model (SM). In addition to a direct observation of the Higgs boson, the Large Hadron Collider (LHC) looks to explore BSM physics. Deviations of rare process observables from SM predictions may be taken as indirect evidence of a new coupling beyond the SM physics [13], which can also be explored at lower energies. The pseudoscalar mesons (for example, η or η') are particularly interesting since their decay to e^+e^- pairs is suppressed by $\alpha^2(10^{-4})$ and by helicity conservation due to the small electron mass ($r^2 = (m_e/m_\eta)^2 \simeq 10^{-6}$) [17]. The branching ratio (B.R.) of $\eta \rightarrow e^+e^-$ is 2.3×10^{-9} according to the SM predictions, however, couplings from BSM physics may increase this B.R. significantly [13]. RHIC offers high-luminosity nucleus-nucleus collisions with large multiplicities and copious hadrons of interest thereby providing a unique environment for studying rare decay processes, nuclear medium effects, and searching for BSM physics. With recent upgrades to the detector [18], including the data acquisition system [19], the STAR Collaboration is able to benefit from a high rate capability as well as excellent lepton identification at low momentum in the search for rare decays.

This paper is organized as follows. Section II shows the detector and data sample used in this analysis. Section III describes the analysis details including electron identification, electron-pair distributions, background subtraction, and di-electron continuum without efficiency correction. Section IV presents the details of the simulations of di-electrons from light-meson decays and heavy-flavor decays, collectively called cocktail simulations. The efficiency correction for di-electron continuum, the corrected di-electron continuum, and systematic uncertainties are also discussed in this section. Results on the yields of ω , ϕ , and J/ψ through di-electronic decays are presented in detail in Sec. V. The rare decay of $\eta \rightarrow e^+e^-$ is discussed in Sec. VI. Lastly, Sec. VII provides a concluding summary.

II. DETECTORS AND DATA SAMPLE

Two sub-detectors are used in this analysis at mid-rapidity at STAR [20]: the Time Projection Chamber (TPC) [21] and a newly installed Time-Of-Flight detector (TOF) [18]. The TPC is the main tracking detector

*deceased

at STAR, measuring momenta, charge, and energy loss of charged particles. The TPC is a 4.2 m long cylinder surrounding the beam pipe covering the space between 50 and 200 cm in radius filled with P10 gas (90% argon and 10% methane). Electrons from ionized gas drift toward the nearest endcap, where the signals are read out. The TPC readout is divided azimuthally into 24 sectors, 12 at each end. Each sector is divided into inner and outer subsectors with a total of 45 pad row readouts. The pad row readouts provide precise positions of primary ionization clusters (hits) generated by charged particles. The ionization energy loss of a charged particle in TPC gas (dE/dx) is used for particle identification [22, 23]. The truncated mean by removing a given fraction (30%) of the clusters having the largest signal, is used to measure the most probable dE/dx . In 2009, 72% of the full TOF system was installed and operational. The full TOF system contains 120 units which we call trays, 60 in the pseudo-rapidity range $0 < \eta < 0.9$ and 60 at $-0.9 < \eta < 0$, with each tray covering 6 degrees in azimuth. The TOF has a typical stop timing resolution of 85 ps allowing the identification of $\pi(K)$ up to a momentum of 1.6 GeV/c and $p(\bar{p})$ up to a momentum of 3 GeV/c [24, 25].

The minimum-bias events were defined by the coincidence of signals in the two Vertex Position Detectors (VPDs) [26], located on each side of the STAR barrel, covering $4.4 < |\eta| < 4.9$. This di-electron analysis used 107 million minimally biased events at $\sqrt{s} = 200$ GeV from non-singly diffractive (NSD) $p + p$ collisions ($\sigma_{NSD} = 30.0 \pm 3.5$ mb [27]), in which collision vertex is required to be within 50 cm around the TPC center along the beam line.

III. DATA ANALYSIS

A. Tracking and particle identification

Hits belonging to charged particles traversing the TPC are collected and reconstructed into tracks with well defined geometry, momentum (p), and dE/dx . Only tracks that project back to within 1 cm of the collision vertex are retained in the analysis thereby limiting the combinatorial background from conversions and enabling a high tracking efficiency. The tracks are required to have at least 25 hits out of a maximum of 45 to avoid split tracks, and a minimum of 15 hits used in the dE/dx measurement to obtain good dE/dx resolution [21, 28]. For particles directly originating from the collision, the collision vertex is then added as an additional hit to further improve the momentum measurement [28].

Figure 1 panel (a) shows the $1/\beta$ from TOF of particles versus momentum in $p + p$ collisions while panel (b) and (c) show the normalized dE/dx ($n\sigma_e$) distribution from the TPC as a function of p_T without and with a requirement of high velocity $|1/\beta - 1| < 0.03$. The $n\sigma_e$ is defined as: $n\sigma_e = \ln(dE/dx/I_e)/R_e$, where dE/dx is the measured specific energy loss of a particle, and I_e is the

expected dE/dx of an electron. R_e is the $\ln(dE/dx/I_e)$ resolution of an electron and is better than 8%. With a perfect calibration, the $n\sigma_e$ for single electrons should follow a standard normal distribution. Electron candidates whose $n\sigma_e$ falls between the lines in Figure 1 panel (c) are selected. Figure 2 shows the $n\sigma_e$ distribution at $0.4 < p_T < 0.5$ GeV/c after the cut of $|1/\beta - 1| < 0.03$. The two dashed lines perpendicular to the x-axis represent the range of the $n\sigma_e$ cut in this p_T region. A Gaussian plus exponential function representing electron and hadron components respectively is used to fit the $n\sigma_e$ distribution. From the fit, we derive the purity and the $n\sigma_e$ cut efficiency on electron candidates as a function of p_T , as shown in Fig. 3. The purity is defined within a range of $n\sigma_e$ (i.e. between the vertical dashed lines in Fig. 2) as being the ratio of the electron counts in the area of dashed Gaussian to the counts of all particles. The efficiency is defined to be the ratio of the electron counts under the dashed Gaussian within $n\sigma_e$ to the total electron counts under the dashed Gaussian. The errors on the efficiency and purity are determined by adjusting the fit range. The electron yields are sensitive to the fit range since the hadron contamination increases in the smaller $n\sigma_e$ region thereby leading to large errors for the efficiency at $p_T > 0.8$ GeV/c. Our exponential extrapolation of the $n\sigma_e$ for hadron component tends to over-estimate the background and therefore should be taken as an upper limit on the hadron contamination. By combining the velocity (β) information from the TOF and the dE/dx from the TPC, electrons can be clearly identified from low to intermediate p_T ($p_T < 3$ GeV/c) at $|\eta| < 1$ [29].

B. Di-electron invariant mass distribution and background subtraction

With a high purity for the electron samples, the e^+ and e^- from the same events are combined to generate the invariant mass distributions (M_{ee}) of e^+e^- pairs called unlike-sign distributions. The unlike-sign distributions contain both signal and background. The signals are di-electrons from light-meson decays and heavy-flavor decays (charmonium and open charm correlation). The background contains the random combinatorial pairs and correlated pairs. The electron candidates are required to be in the range of $|\eta| < 1$ and $p_T > 0.2$ GeV/c while e^+e^- pairs are required to be in the rapidity range of $|y_{ee}| < 1$.

Two methods are used for background estimation, based on same-event like-sign and mixed-event unlike-sign techniques. In the like-sign technique, electron pairs with the same charge sign are combined from the same events. In the mixed-event technique, unlike-sign pairs are formed from different events. In order to ensure the events which are mixed have similar geometric acceptance in the detector, we only mix events which have collision vertices within 5 cm of each other along the beam line direction.

Neither method represents the background perfectly.

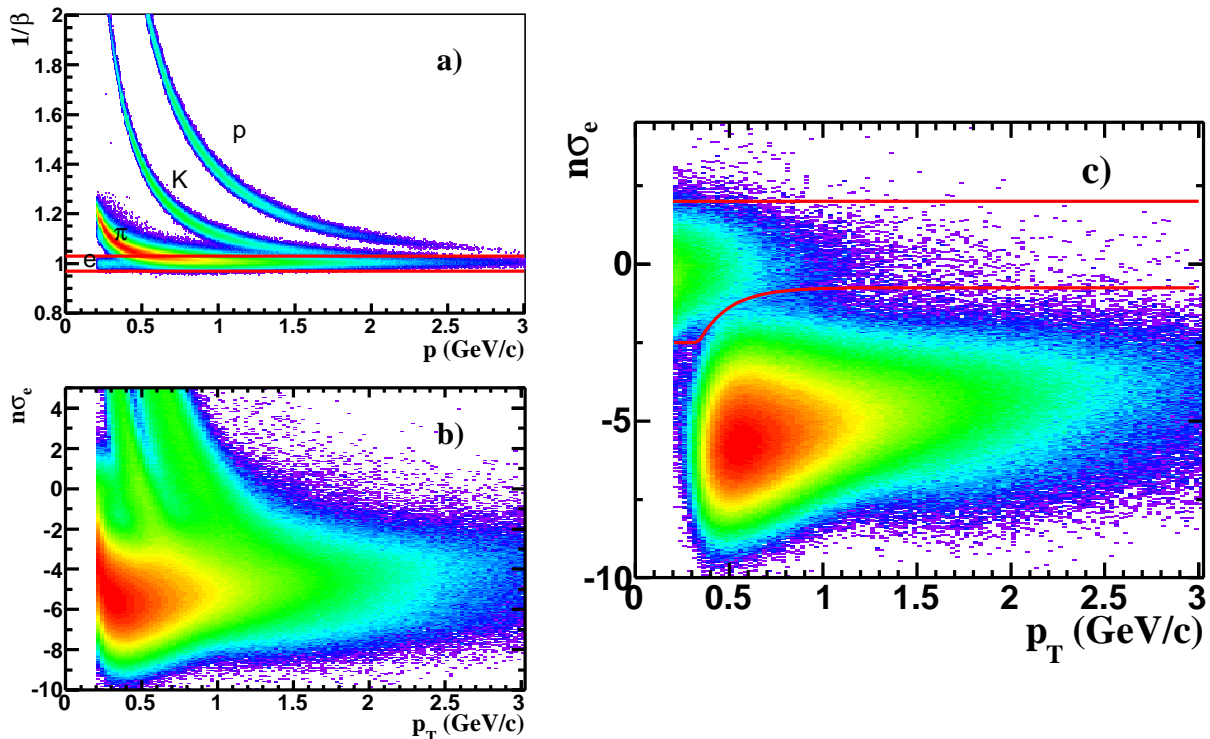


FIG. 1: (Color online) Panel (a): $1/\beta$ versus momentum of tracks from 200 GeV $p + p$ collisions from the TOF at $|\eta| < 1$. The red line indicates the cut of $|1/\beta - 1| < 0.03$. Panel (b): The normalized dE/dx distribution from the TPC as a function of p_T . Panel (c): The normalized dE/dx distribution from the TPC as a function of p_T with the cut of $|1/\beta - 1| < 0.03$. An electron band is prominent with the requirement of velocity close to the speed of light from TOF measurement.

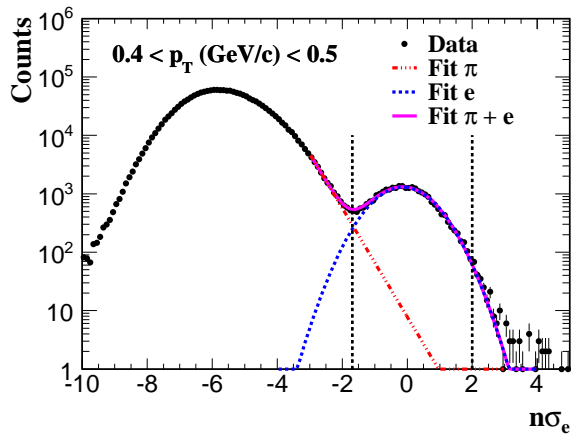


FIG. 2: (Color online) The $n\sigma_e$ distribution in $0.4 < p_T < 0.5$ GeV/c after the cut of $|1/\beta - 1| < 0.03$. The solid curve represents a Gaussian plus exponential fit to the $n\sigma_e$ distribution. The dot-dashed line is for the hadron component and the dashed is for the electron contribution. The two dashed lines perpendicular to the x-axis represent the range of the $n\sigma_e$ cut to ensure a high purity for electron candidates in this p_T range.

In the low-mass region, there is a correlated cross pair background (coming from two pairs of e^+e^- from the same meson decays: Dalitz decays followed by a conversion of the decay photon, or conversions of multiple photons from the same meson). This background is present in the like-sign distribution but not in the mixed-event background. On the other hand, due to the sector structure of detectors and the different curvatures of positively and negatively charged particle tracks in the transverse plane in magnetic field, like-sign and unlike-sign pairs will have different acceptance. Moreover, in the high invariant mass range, there may be contributions from jet correlations which are absent from the mixed-event technique.

Figure 4 shows the invariant mass distribution for unlike-sign pairs, like-sign pairs, and mixed-event background. The mixed-event distribution is normalized by a constant to match the like-sign distribution in the mass region of $0.4-1.5$ GeV/ c^2 . We subtract the like-sign background at $M_{ee} < 0.4$ GeV/ c^2 and mixed-event background in the higher-mass region. At higher mass, we compare the shape of like-sign and mixed-event distributions. A constant is used to fit the ratio of like-sign over mixed-event distributions at $M_{ee} > 0.4$ GeV/ c^2 and the χ^2/NDF is 14/15, as shown in the ratio plot in Fig. 5 (a).

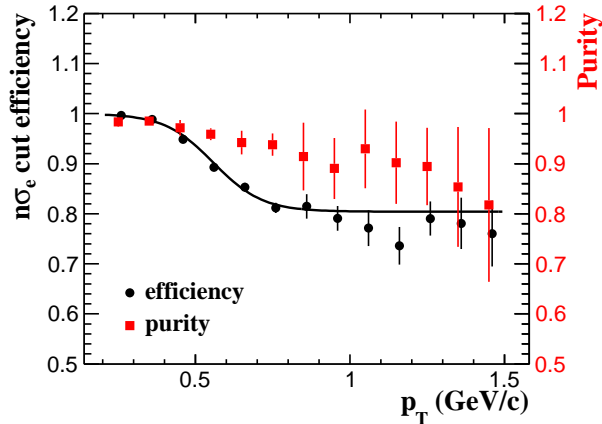


FIG. 3: (Color online) The purity and the $n\sigma_e$ cut efficiency for electron candidates as a function of p_T in $|\eta| < 1$ for $p + p$ collisions at $\sqrt{s} = 200$ GeV. The squares represent the purity and closed circles represent the $n\sigma_e$ efficiency. The p_T positions of the last three data points for the efficiency are slightly shifted for clarity. The error bars are the quadrature sum of statistical and systematic uncertainties. The line is a fit to the efficiency data points and used for the efficiency correction. A constant component in the fit at $p_T > 0.8$ GeV/ c is driven by the study in Ref. [23].

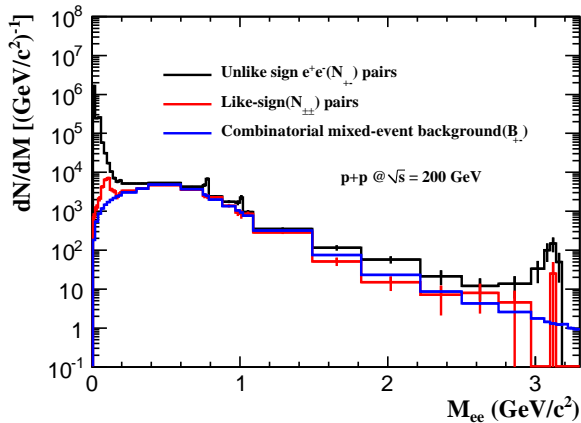


FIG. 4: (Color online) The electron-pair invariant mass distributions for unlike-sign pairs, like-sign, and mixed-event (combinatorial) background in minimum-bias $p + p$ collisions. The electron candidates are required to be in the range of $|\eta| < 1$ and have a p_T greater than 0.2 GeV/ c . The ee pairs were required to be in the rapidity range of $|y_{ee}| < 1$. The uneven bin widths are used based on the yields and the signal to background ratios.

We also find that with a significantly higher transverse momentum for the pair from the Barrel Electro-Magnetic Calorimeter triggered events, the shapes of like-sign and mixed-event distributions agree in the mass region of $1-3$ GeV/ c^2 [30]. Fig. 5 (b) shows the distribution of the difference of the azimuthal angles ($\Delta\phi$) of the two electrons in the unlike-sign, like-sign and mixed-event pairs. The difference between like-sign and mixed-event pairs at low $\Delta\phi$ can be attributed to cross-pair contributions. By selecting $M_{ee} > 0.4$ GeV/ c^2 , the $\Delta\phi$ distributions of like-sign and mixed-event pairs match nicely with each other as shown in Fig. 5 (c), indicating that mixed-event background subtraction is valid in the corresponding mass region.

In addition, we subtract the like-sign background in the whole mass region as a cross-check. The difference in the di-electron yields from the mixed-event and like-sign methods is within the error bar on the two distributions at $M_{ee} > 0.4$ GeV/ c^2 . We correct for acceptance differences between the like-sign and unlike-sign electron pairs in both methods and will discuss the detail in Sec. IV C.

Figure 6 (a) shows the di-electron continuum after background subtraction from like-sign and mixed-event methods in $p + p$ collisions at $\sqrt{s} = 200$ GeV. The measurements are done requiring $|y_{e^+e^-}| < 1$, $|\eta_e| < 1$ and $p_T(e) > 0.2$ GeV/ c and no efficiency correction has been applied. The two methods give consistent results for $M_{ee} > 0.4$ GeV/ c^2 . For the following, we use the yields from like-sign method for $M_{ee} < 0.4$ GeV/ c^2 and results obtained from the mixed-event method at higher mass as the default since the mixed-event background distribution matches the like-sign distribution and has better precision at $M_{ee} > 0.4$ GeV/ c^2 . The signal to background ratio in $p + p$ collisions versus M_{ee} is shown in Fig. 6 (b).

IV. DI-ELECTRON CONTINUUM IN STAR ACCEPTANCE

A. Cocktail simulation

The di-electron pairs may come from decays of the light-flavor and heavy-flavor hadrons. They include π^0 , η , and η' Dalitz decays: $\pi^0 \rightarrow \gamma e^+e^-$, $\eta \rightarrow \gamma e^+e^-$, and $\eta' \rightarrow \gamma e^+e^-$; vector meson decays: $\omega \rightarrow \pi^0 e^+e^-$, $\omega \rightarrow e^+e^-$, $\rho^0 \rightarrow e^+e^-$, $\phi \rightarrow \eta e^+e^-$, $\phi \rightarrow e^+e^-$, and $J/\psi \rightarrow e^+e^-$; heavy-flavor hadron semi-leptonic decays: $c\bar{c} \rightarrow e^+e^-$ and $b\bar{b} \rightarrow e^+e^-$; and Drell-Yan contributions. We fit the invariant yields of measured mesons with the Tsallis functions [31], as shown in Fig. 7 (a). We use the Tsallis functions as input to a detector simulation in which the particles are decayed into di-electrons with the appropriate B.R.s. This GEANT detector simulation [32] uses a detailed description of the STAR geometry in 2009. Simulated e^+e^- cocktails from the various contributing sources, as shown in Fig. 7 (b), are selected using the same cut conditions as those in the analyses of real events. The di-electron contributions from the

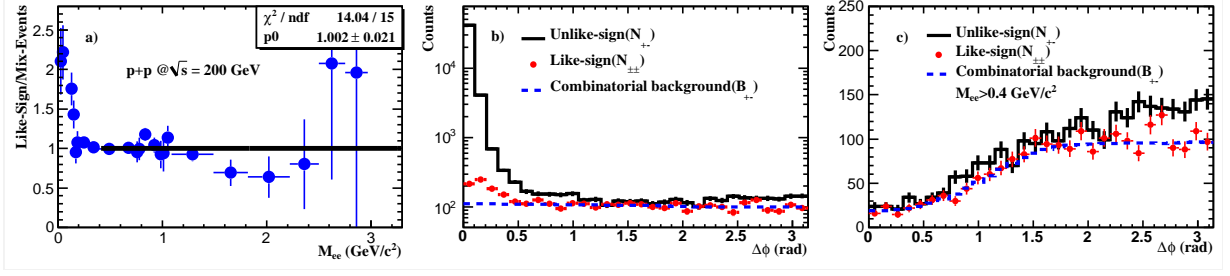


FIG. 5: (Color online) Panel (a): The ratio of like-sign to mixed-event distributions in minimum-bias $p+p$ collisions. Panel (b): The distribution of the difference of the azimuthal angles ($\Delta\phi$) of the two electrons in the unlike-sign, like-sign and mixed-event pairs in minimum-bias $p+p$ collisions. Panel (c): The $\Delta\phi$ distributions of unlike-sign, like-sign and mixed-event pairs for $M_{ee} > 0.4 \text{ GeV}/c^2$ in minimum-bias $p+p$ collisions. Errors are statistical.

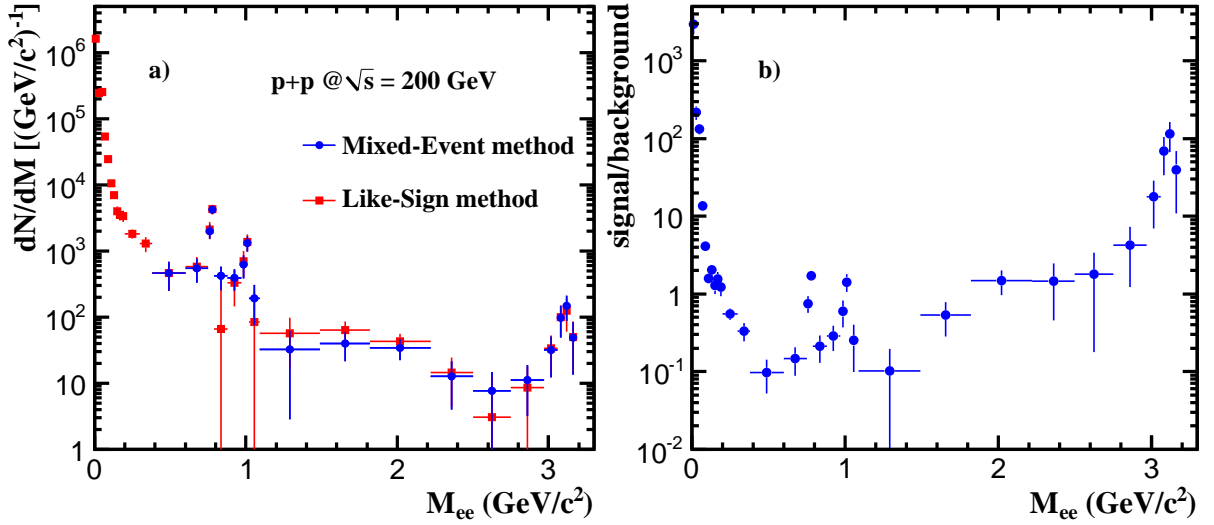


FIG. 6: (Color online) Panel (a): The di-electron (e^+e^-) continuum after background subtraction without efficiency correction in $\sqrt{s} = 200 \text{ GeV}$ minimum-bias $p+p$ collisions. Errors are statistical only. Panel (b): The signal over background ratio as a function of M_{ee} in NSD $p+p$ collisions at $\sqrt{s} = 200 \text{ GeV}$. Errors are statistical.

gamma conversion $\gamma \rightarrow e^+e^-$ in the detector material are accepted in both data and simulation subject to the same analysis cuts as well. The imperfect description of the material in the simulation leads to 3% systematic uncertainty for the cocktail simulation at $M_{ee} < 0.1 \text{ GeV}/c^2$. The Dalitz decays of $\eta \rightarrow \gamma^0 e^+e^-$, $\omega \rightarrow \pi^0 e^+e^-$ and $\eta' \rightarrow \gamma e^+e^-$ are obtained using the Kroll-Wada expression [33]. The $\rho^0 \rightarrow e^+e^-$ line shape is convoluted with the Boltzmann phase space factor [34, 35].

For the Dalitz decays of π^0 , η and η' , we use the formula

$$\frac{dN}{dM_{ee}} \propto \sqrt{1 - \frac{4m_e^2}{M_{ee}^2}} \left(1 + \frac{2m_e^2}{M_{ee}^2}\right) \frac{1}{M_{ee}} \left(1 - \frac{M_{ee}^2}{M_h^2}\right)^3 |F(M_{ee}^2)|^2, \quad (1)$$

in which, m_e is the electron mass, M_{ee} is the di-electron mass, and M_h is the mass of the hadron which decays into the di-electron. $F(M_{ee}^2)$ is the electro-magnetic transition form factor. For the Dalitz decays of vector mesons ω and ϕ ($A \rightarrow Be^+e^-$), the formula is

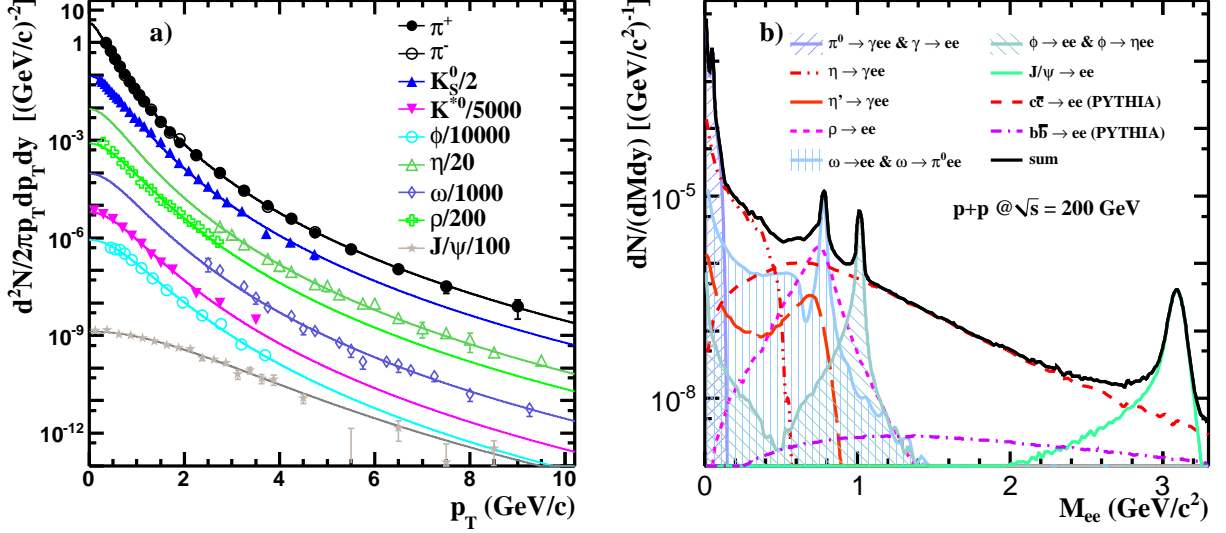


FIG. 7: (Color online) Panel (a): The invariant yields of measured mesons fit with the Tsallis functions [31] in $p+p$ collisions at $\sqrt{s} = 200$ GeV. Panel (b): The simulated raw di-electron continuum within STAR acceptance for $\sqrt{s} = 200$ GeV minimum-bias $p+p$ collisions. Different cocktail contributions are shown.

$$\frac{dN}{dM_{ee}} \propto \sqrt{1 - \frac{4m_e^2}{M_{ee}^2}} \left(1 + \frac{2m_e^2}{M_{ee}^2}\right) \frac{1}{M_{ee}} \left[\left(1 + \frac{M_{ee}^2}{M_A^2 - M_B^2}\right)^2 - \frac{4M_A^2 M_{ee}^2}{(M_A^2 - M_B^2)^2} \right]^{3/2} |F(M_{ee}^2)|^2, \quad (2)$$

in which the M_A and M_B are the mass of particle A and B, respectively. The form factor is parameterized as

$$F(M_{ee}^2) = \frac{1}{1 - M_{ee}^2 \Lambda^{-2}}, \quad (3)$$

in which Λ^{-2} is the form factor slope. This is used for most of the Dalitz decays except for $\eta' \rightarrow \gamma e^+ e^-$. For η' , the parametrization is from [17]:

$$|F(M_{ee}^2)|^2 = \frac{1}{(1 - M_{ee}^2 \Lambda^{-2})^2 + \Gamma_0^2 \Lambda^{-2}}. \quad (4)$$

The Γ_0^2 is $1.99 \times 10^{-2} (\text{GeV}/c^2)^2$. The Λ parameters are listed in Table I. The $\rho^0 \rightarrow e^+ e^-$ line shape is given by:

$$\frac{dN}{dM_{ee} dp_T} \propto \frac{M_{ee} M_\rho \Gamma_{ee}}{(M_\rho^2 - M_{ee}^2)^2 + M_\rho^2 (\Gamma_{\pi\pi} + \Gamma_{ee} \Gamma_2)^2} \times PS, \quad (5)$$

$$\Gamma_{\pi\pi} = \Gamma_0 \frac{M_\rho}{M_{ee}} \left(\frac{M_{ee}^2 - 4M_\pi^2}{M_\rho^2 - 4M_\pi^2} \right)^{3/2}, \quad (6)$$

$$\Gamma_{ee} = \Gamma_0 \frac{M_\rho}{M_{ee}} \left(\frac{M_{ee}^2 - 4m_e^2}{M_\rho^2 - 4m_e^2} \right)^{1/2}, \quad (7)$$

where M_ρ is $776 \text{ MeV}/c^2$, M_π is the π mass, Γ_0 is $149 \text{ MeV}/c^2$, Γ_2 is the B.R. of $\rho^0 \rightarrow e^+ e^-$, PS is the Boltzmann phase space factor, and T is 160 MeV , the inverse slope parameter [34]. The possible small contribution from the interference effect [40] between ρ^0 and ω is not considered.

The invariant yield of π^0 is taken as the average of π^+ and π^- [25, 41]. The yields of ϕ [42] and ρ^0 [35] are from STAR while the η [43], ω [44] and J/ψ [45] yields are measured by PHENIX. Table I lists the total yields at mid-rapidity ($dN/dy|_{y=0}$) in 200 GeV NSD $p+p$ collisions. The $c\bar{c}$ cross section is another input to the cocktail simulation, and has been constrained by the published low- p_T D^0 spectrum in 200 GeV d+Au collisions [29], the non-photonic electron spectrum in 200 GeV $p+p$ collisions [46], and the di-electron continuum in this analysis. The details of these constraints will be shown in Sec. IV C. The $e^+ e^-$ shapes from open heavy-flavor pairs are obtained using PYTHIA6.416, in which k_T factor PARP(91)=1 GeV/c , and parton shower PARP(67)=1. With these parameters chosen, PYTHIA

TABLE I: The total yields at mid-rapidity dN/dy from Tsallis fit, decay B.R.s, and Λ parameters of hadrons in NSD $p + p$ collisions at $\sqrt{s} = 200$ GeV.

meson	$\frac{dN}{dy}$	relative uncertainty	decay channel	B.R.	$\Lambda^{-2} (\text{GeV}/c^2)^{-2}$
π^0	1.28	14%	γe^+e^-	1.174×10^{-2}	1.756 ± 0.022 [36]
η	1.7×10^{-1}	23%	γe^+e^-	7.0×10^{-3}	1.95 ± 0.18 [37]
ρ	2.2×10^{-1}	15%	e^+e^-	4.72×10^{-5}	–
ω	1.3×10^{-1}	21%	e^+e^-	7.28×10^{-5}	–
ω			$\pi^0 e^+e^-$	7.7×10^{-4}	2.24 ± 0.06 [37]
ϕ	1.7×10^{-2}	20%	e^+e^-	2.954×10^{-4}	–
ϕ			ηe^+e^-	1.15×10^{-4}	3.8 ± 1.8 [38]
η'	4.1×10^{-2}	29%	γe^+e^-	4.7×10^{-4} [39]	1.8 ± 0.4 [17]
J/ψ	2.4×10^{-5}	15%	e^+e^-	5.94×10^{-2}	–

can describe the shape of STAR measured D^0 spectrum and non-photonic electron spectrum. The total contribution from the simulation is shown as the black solid curve in Fig. 7 (b). In the intermediate mass region, the di-electron continuum is dominated by the $c\bar{c}$ contribution.

B. Efficiency and acceptance correction

For the di-electron continuum, the efficiency corrections are applied within the STAR acceptance of $|y_{e^+e^-}| < 1$, $|\eta_e| < 1$ and $p_T(e) > 0.2$ GeV/ c . The single electron efficiency includes the TPC tracking efficiency, TOF acceptance and detector response, and the dE/dx efficiency. Single electron tracking efficiency and acceptance in the TPC are determined by Monte Carlo GEANT simulations. The TOF acceptance and response efficiency for electrons is found to be 46% independent of p_T for $|\eta| < 1$ [25]. The efficiency of the $n\sigma_e$ cut, used to ensure a high purity for electron sample, is close to 100% at low p_T and falls to $\sim 80\%$ by $p_T = 0.8$ GeV/ c , as shown in Fig. 3.

Figure 8 shows the efficiency for single electrons in the pseudo-rapidity range of $|\eta| < 1$ in $p + p$ collisions at $\sqrt{s} = 200$ GeV. Open circles represent the TPC tracking efficiency alone. Including TOF matching and response decreases the efficiency as shown by the triangles. With additional dE/dx cuts, the final efficiency for single electrons at $|\eta_e| < 1$ is shown as squares. In $p + p$ collisions, 72% out of 120 TOF trays were installed and the efficiency dependence on azimuthal angle is shown in Fig. 9 for positive and negative η regions. We have accounted for the incomplete TOF acceptance in determining efficiencies for the di-electron spectra.

The efficiency factor for the di-electron continuum within STAR's acceptance is obtained in two steps. We obtain the input cocktail A within STAR acceptance by the method described in Sec. IV A. The input cocktail includes the radiation energy loss and momentum resolution determined from GEANT simulations. The result is shown by the solid line in Fig. 10 (a). Then we obtain cocktail B from GEANT simulations with proper

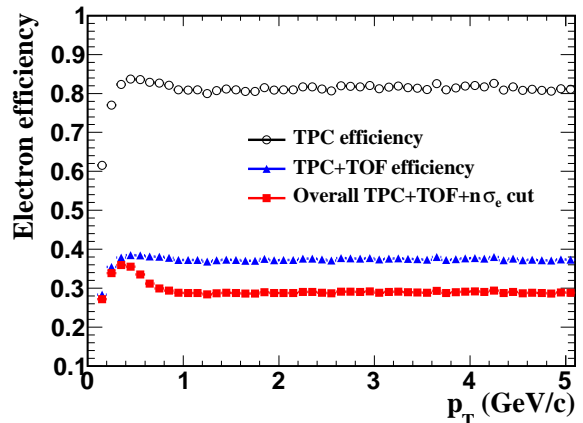


FIG. 8: (Color online) The efficiency for single electrons as a function of p_T in the pseudo-rapidity range of $|\eta| < 1$ in $p + p$ collisions at $\sqrt{s} = 200$ GeV. Open circles represent the TPC tracking efficiency. With additional TOF matching and response, the efficiency is shown as triangles. With additional dE/dx cuts, the final efficiency is shown as squares.

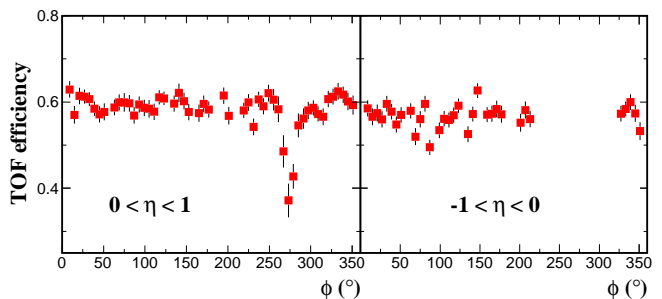


FIG. 9: (Color online) The TOF efficiency as a function of azimuthal angle in the positive and negative η region. The hole in the negative η region corresponds to the 28% trays that still needed to be installed in 2009. The 3 trays at around 270 degree in the positive η region have smaller matching efficiencies but have similar performances in other aspects.

efficiency factors including the TPC tracking, TOF acceptance and response, and dE/dx cut for single electrons as described above, and shown as the dashed line in Figure 10 (a). The ratio of these two is the efficiency factor for the di-electrons and is shown in Fig. 10 (b) in $p + p$ collisions at $\sqrt{s} = 200$ GeV. The final di-electron continuum within the STAR acceptance is obtained after this correction is applied and is discussed in Sec. IV C. The uncertainty on this factor is about 10% with a negligible p_T dependence.

C. Results

The systematic uncertainties on the di-electron continuum are dominated by background subtraction (acceptance difference between like-sign and unlike-sign electron pairs and normalization of mixed-event distributions) and hadron contamination. The acceptances of the like-sign and unlike-sign distributions are the same within 5% at $M_{ee} > 0.1$ GeV/ c^2 due to the azimuthal symmetry and solenoidal magnetic field. The small acceptance differences due to track merging, sector boundaries, and dead channels have been evaluated using the unlike-sign distribution and the like-sign distribution from the mixed-event technique. This difference is included in the systematic uncertainty. In addition, for $M_{ee} > 0.4$ GeV/ c^2 , the normalization factor between the mixed-event and the like-sign distributions contributes 0-7% to the overall uncertainty. The systematic uncertainty from efficiency factors is about 10% with no significant mass dependence. The uncertainties in hadron contamination (hadrons from resonance decays mis-identified as electrons) are 0-32% and are mass dependent. Figure 11 shows the relative systematic uncertainties from different sources for each mass bin. The normalization uncertainty in NSD $p + p$ collisions is 8% [46]. Additional normalization uncertainty in VPD triggered minimum-bias events taking into account the trigger bias and vertex finding efficiency is 8%, determined by using PYTHIA simulations [47]. The total normalization uncertainty for di-electron mass spectra is 11% in $p + p$ collisions. Table II shows the systematic uncertainties from different sources.

The uncertainties on the cocktail simulations include the decay form factors and the measured cross section for each hadron. By fitting the di-electron continuum, open charm [29] and non-photonic electron spectra [46] simultaneously, we find that the $c\bar{c}$ cross section in 200 GeV $p + p$ collisions is $0.92 \pm 0.10 \pm 0.26$ mb, consistent with early RHIC measurements [29, 48]. This is used to generate the charm component in this paper. The systematic uncertainties for the cocktail simulation as a function of mass are shown in Fig. 11. Future precise measurements of di-electron continuum in the intermediate mass region can further constrain the charm production mechanism in $p + p$ collisions.

After the efficiency correction, the di-electron contin-

TABLE II: Systematic uncertainties from different sources for di-electron continuum.

source	contribution factors
background subtraction	0-27%
contamination	0-32%
efficiency	10%
total normalization	11%
cocktail simulation	14-33%

uum within the STAR acceptance is shown in Fig. 12 for 200 GeV NSD $p + p$ collisions. The di-electron mass spectrum is not corrected for momentum resolution and radiation energy loss effect. The ratio of data to cocktail simulation is shown in the lower panel. Within the uncertainties, the cocktail simulation is consistent with the measured di-electron continuum. The χ^2/NDF between data and cocktail simulation are 21/26 at $M_{ee} > 0.1$ GeV/ c^2 and 8/7 at $1.1 < M_{ee} < 3.0$ GeV/ c^2 .

V. VECTOR MESON PRODUCTION

The yields of the ω , ϕ and J/ψ long-lived vector mesons can be extracted from the di-electron continuum. We use the mixed-event technique to reconstruct the combinatorial background beneath the respective peaks. The mixed-event distribution is normalized by a constant to match the like-sign distribution in the mass region of 0.4-1.5 GeV/ c^2 , as discussed in Sec. III B. The background is then subtracted to obtain the signal, which will contain some additional residual background of di-electron pairs from other sources described in Sec. IV A.

A two-component fit is used to extract the residual background subtracted $\omega \rightarrow e^+e^-$ raw signal in the invariant mass range of $0.7 < M_{ee} < 0.85$ GeV/ c^2 . The first component represents the line shape (the $\omega \rightarrow e^+e^-$ signal shape), the second the residual background. The line shape of $\omega \rightarrow e^+e^-$ invariant mass distribution, and the shape and magnitude of the background are determined from the simulations described in Sec. IV A. The systematic uncertainties of the $\omega \rightarrow e^+e^-$ raw yields are derived by changing the magnitude of the background allowed by the uncertainties of the cocktail simulation and the analysis cuts. The total contribution to the raw yield is about 20%. Figure 13 shows the fit to the M_{ee} distribution at $0.7 < M_{ee} < 0.85$ GeV/ c^2 in three different p_T bins for $p + p$ collisions at $\sqrt{s} = 200$ GeV.

In order to present the final differential invariant cross section as a function of p_T , the raw vector meson yield ($\omega \rightarrow e^+e^-$) is corrected for acceptance and all detector effects, which reduce the measured raw yield relative to the actual yield. The total efficiency correction for $\omega \rightarrow e^+e^-$ at $|y| < 1$ is shown in Fig. 14. We use the simulations described in Sec. IV A to determine this correction, which accounts for limits in TPC acceptance and inefficiencies in TPC tracking, limits in the TOF acceptance/response, and the rejection of signal due to the

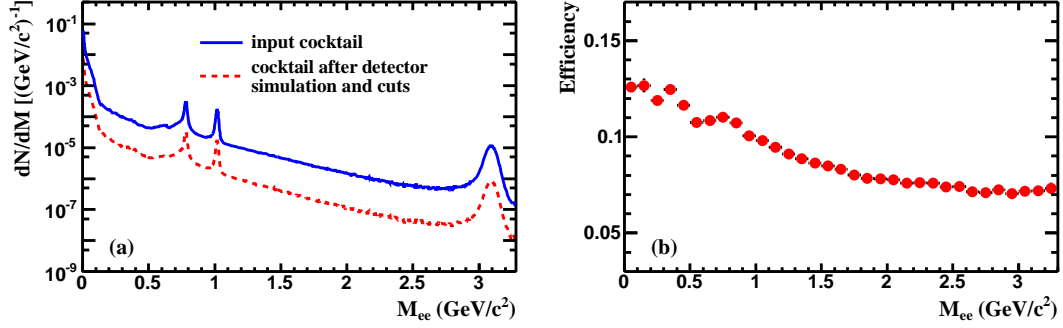


FIG. 10: (Color online) (a) The M_{ee} distribution within STAR's acceptance ($|y_{e^+e^-}| < 1$, $|\eta_e| < 1$, and $p_T(e) > 0.2$ GeV/c) from simulation. The solid line represents the input cocktail. The dashed line represents the cocktail from GEANT simulations taking into account the proper efficiency factors described in the text. (b) The efficiency of di-electron continuum as a function of M_{ee} within the STAR acceptance in $p + p$ collisions at $\sqrt{s} = 200$ GeV.

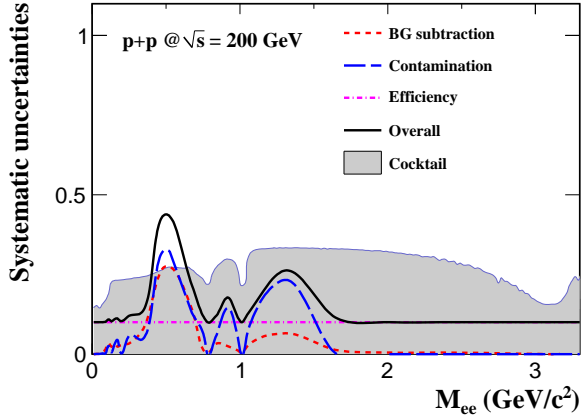


FIG. 11: (Color online) Systematic uncertainties as a function of mass from different source contributions. Also shown are the systematic uncertainties of the cocktail simulation.

dE/dx cut. The invariant yield is defined as follows:

$$\frac{d^2N}{2\pi p_T dp_T dy} = \frac{N_{raw} \times NORM}{2\pi p_T dp_T dy \times N_{event} \times \epsilon \times B.R.}, \quad (9)$$

where N_{raw} represents the raw signal counts, N_{event} is the total event number, ϵ is the total efficiency and acceptance correction factor, $B.R.$ is the branching ratio for $\omega \rightarrow e^+e^-$, and $NORM$ is the normalization factor ($64 \pm 5\%$ for VPD triggered minimum-bias events taking into account the trigger bias and vertex finding efficiency, determined by and corrected for using PYTHIA [47] simulations). The ω invariant yield in NSD $p + p$ collisions at $\sqrt{s} = 200$ GeV is presented in Fig. 15. The systematic uncertainties are dominated by uncertainties in the two-component fit, and uncertainties in total efficiency which are also described in Sec. IV A. Table III lists the detailed systematic uncertainties for ω yields from difference sources. Our ω yields from di-electron decays are consistent with previous results [49] and a prediction

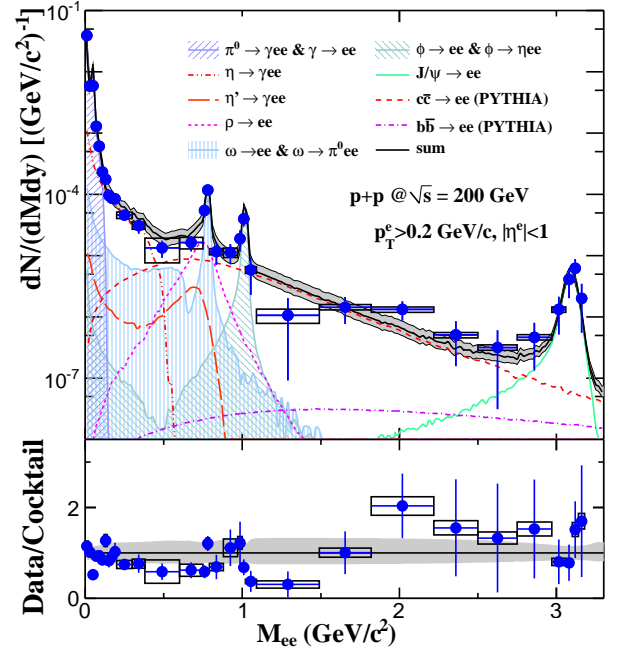


FIG. 12: (Color online) The comparison for di-electron continuum between data and simulation after efficiency correction within the STAR acceptance in $\sqrt{s} = 200$ GeV NSD $p + p$ collisions. The di-electron continuum from simulations with different source contributions is also shown. The statistical errors are shown as bars. The systematic uncertainties are shown as boxes. The 11% normalization uncertainty on data is not shown. The band on top of the solid curve illustrates the systematic uncertainties on cocktail simulation.

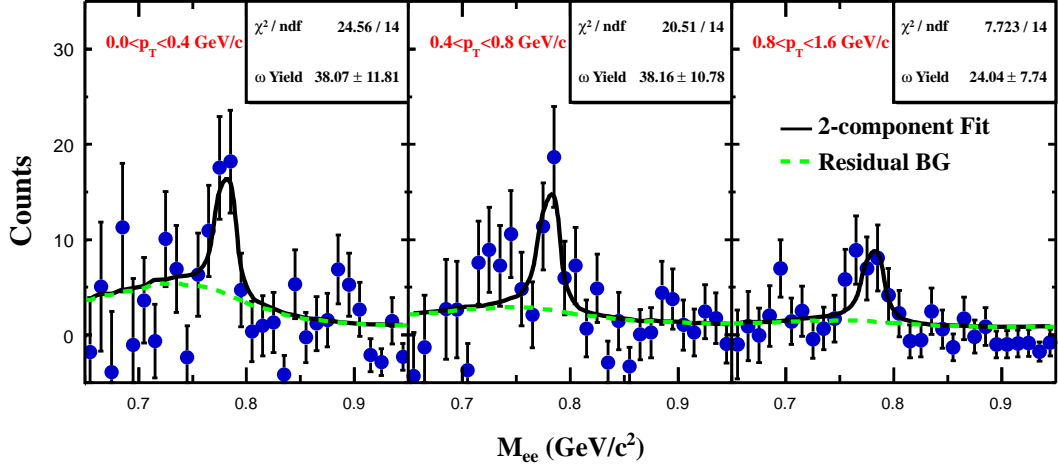


FIG. 13: (Color online) The M_{ee} distribution for three different p_T bins after the mixed-event background subtraction at $0.65 < M_{ee} < 0.95$ GeV/c^2 in $p+p$ collisions at $\sqrt{s} = 200$ GeV . The curves represent fits in the range of $0.7 < M_{ee} < 0.85$ GeV/c^2 . Errors on data points are statistical.

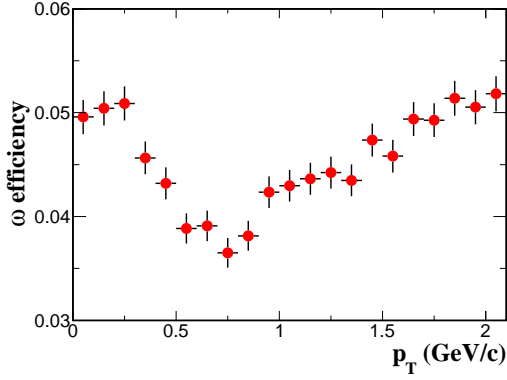


FIG. 14: (Color online) The efficiency including STAR acceptance for $\omega \rightarrow e^+e^-$ at $|y| < 1$ in $p+p$ collisions at $\sqrt{s} = 200$ GeV .

TABLE III: Systematic uncertainties from different sources for ω yields.

source	contribution factors
two component fit	9-16%
$n\sigma_e$ cut	3-7%
efficiency	10%
total normalization	11%

from a Tsallis fit, which fits spectra of other particles and high p_T ω yields [31, 44]. We obtain a mid-rapidity dN/dy of 0.10 ± 0.02 (stat.) ± 0.02 (sys.) for ω .

In addition to $\omega \rightarrow e^+e^-$ yields, we also obtain the mid-rapidity yields, dN/dy , for the ϕ and J/ψ particles in NSD $p+p$ collisions at $\sqrt{s} = 200$ GeV . Due to limited statistics, the invariant mass signal can only be extracted

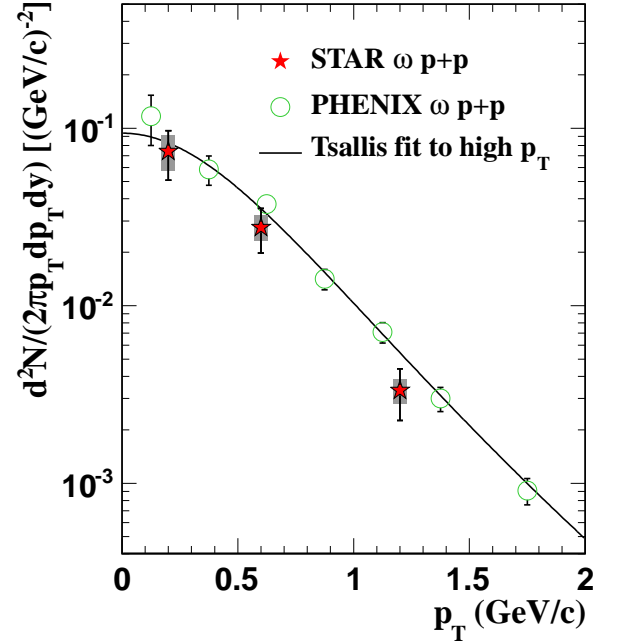


FIG. 15: (Color online) The $\omega \rightarrow e^+e^-$ invariant yield, divided by its B.R., in NSD $p+p$ collisions at $\sqrt{s} = 200$ GeV . The circles represent PHENIX published results [49]. The bars are statistical errors and boxes are systematic uncertainties. A normalization uncertainty of 11% is not shown. The yields at the center of the p_T bin are corrected for bin width effect. The line represents the yields of ω from Tsallis function fit to high p_T ω yields measured from its hadronic decay and described in Sec. IV A.

TABLE IV: Systematic uncertainties from different sources for ϕ and J/ψ dN/dy .

source	contribution factors for ϕ	for J/ψ
two component fit	10%	7%
$n\sigma_e$ cut	8%	27%
efficiency	10%	10%
total normalization	11%	11%

over all p_T , rather than individual bins for each particle. As before, we use the two-component fit in the region of M_{ee} at $0.98 < M_{ee} < 1.04$ GeV/ c^2 for the $\phi \rightarrow e^+e^-$, and $3 < M_{ee} < 3.16$ GeV/ c^2 for $J/\psi \rightarrow e^+e^-$. The line shapes of $\phi \rightarrow e^+e^-$ and $J/\psi \rightarrow e^+e^-$ are from simulations as discussed in Sec. IV A. The residual background shape and magnitude are obtained from the cocktail simulation, shown in Sec. IV A. The systematic uncertainties of the ϕ and J/ψ dN/dy due to the residual background are evaluated by changing the magnitude of the background allowed by the uncertainties of the cocktail simulation. The total efficiency correction for each particle is evaluated in the same way as for the $\omega \rightarrow e^+e^-$ analysis. Since the correction depends on p_T , we calculate a weighted average using the predicted spectra from the previously mentioned Tsallis fit as p_T weights. The total efficiency and acceptance correction factors for ϕ and J/ψ are 4.4% and 3.4%, respectively. The systematic uncertainty on the total efficiency correction is about 10%. The normalization uncertainty is 11% in $p + p$ collisions. Table IV lists the detailed systematic uncertainties for the ϕ and J/ψ dN/dy from difference sources. Figure 16 shows the fits to the M_{ee} distributions used to obtain the mid-rapidity yields dN/dy for ϕ and J/ψ in NSD $p + p$ collisions at $\sqrt{s} = 200$ GeV. The final yields in those fits are subject to the total efficiency correction. The dN/dy for ϕ is 0.010 ± 0.002 (stat.) ± 0.002 (syst.), consistent with the measurements from $\phi \rightarrow K^+K^-$ [42, 50]. The dN/dy for J/ψ is $(2.1 \pm 0.7$ (stat.) ± 0.7 (syst.)) $\times 10^{-5}$, consistent with previous measurements [45, 51].

VI. THE RARE DECAY: $\eta \rightarrow e^+e^-$

As discussed in previous section and shown in Fig. 12, the cocktail can describe the data reasonably well around the η mass without the $\eta \rightarrow e^+e^-$ decay channel. We zoom into the low-mass range and show the data and cocktail comparison in Fig. 17. The dot-dashed peak is the $\eta \rightarrow e^+e^-$ contribution with the upper limit of its B.R. from the PDG [36], which is 2.7×10^{-5} [52]. The dashed curve is a two-component fit with the $\eta \rightarrow e^+e^-$ decay channel included. The fit function is

$$A \times N_\eta + B \times \text{Cocktail}, \quad (10)$$

in which N_η is the expected η contribution with the line shape of $\eta \rightarrow e^+e^-$ after detector simulation, *Cocktail* is the expected cocktail contribution described in Sec. IV A

without $\eta \rightarrow e^+e^-$, and A and B are fit parameters. The A and B represent the B.R. for the $\eta \rightarrow e^+e^-$ and a scale factor for the cocktail contribution, respectively. The solid curve shown in Fig. 17 represents the $\eta \rightarrow e^+e^-$ contribution from the fit. It gives the B.R. of the $\eta \rightarrow e^+e^-$ to be $(-9.6 \pm 5.9$ (stat.) ± 5.3 (syst.)) $\times 10^{-6}$. The negative value of B.R. of the $\eta \rightarrow e^+e^-$ is due to the statistical fluctuation at $M_{ee} = 0.55$ GeV/ c^2 . The systematic uncertainties are dominated by background subtraction (34%, the difference between mixed event background subtraction and like-sign subtraction), electron purity (31%, varying the $n\sigma_e$ cuts), and track quality cut (27%, changing the cut of distance of closest approach between the track and the collision vertex).

In addition, although the Dalitz decay yield of $\eta \rightarrow \gamma e^+e^-$ is consistent with the cocktail expectation from the Tsallis fit to η measurements at $p_T > 2$ GeV/ c described in Sec. IV A, the nominal value from the fit in Fig. 17 is about 56% of the input cocktail ($B=56\%$). This is equivalent to a smaller value of N_η and has to be taken into account when the upper limit at the 90% Confidence Level (CL) for the B.R. of $\eta \rightarrow e^+e^-$ is estimated.

With different background subtraction, electronic purity, and track quality cuts, we repeat the fit process described above to obtain the parameter A , the B.R. of the $\eta \rightarrow e^+e^-$. The difference of the A values is attributed to the systematic uncertainties. In this fit procedure, we find that cut conditions do not contribute to the point-to-point variation around η mass range and the statistical error of the parameter A remains unchanged. Therefore, the significance of an observable signal above the background only depends on the statistical fluctuation. To estimate the upper limit for the B.R. of $\eta \rightarrow e^+e^-$ at the 90% CL due to a possible statistical fluctuation, we utilize the statistical error 5.9×10^{-6} for the B.R. of the $\eta \rightarrow e^+e^-$ from the fit and set the lower bound of the B.R. of $\eta \rightarrow e^+e^-$ to be zero instead of the negative value from the fit. The upper limit is found to be $5.9 \times 10^{-6} \times 1.65/0.56 = 1.7 \times 10^{-5}$, in which 1.65 is the upper endpoint of a confidence interval (the lower endpoint is zero) with a 90% CL for a standard normal distribution.

These results provide a promising first glimpse of a program on searching for rare decays of hadrons produced in relativistic heavy-ion collisions at STAR. With large hadron yields to tape, high efficiency for electrons at low momentum and high mass resolution, STAR provides a unique tool for such a program in the years to come.

VII. SUMMARY

The di-electron continuum is measured in $\sqrt{s} = 200$ GeV non-singly diffractive $p + p$ collisions within the STAR acceptance. The cocktail simulations are consistent with the data and provide a reference for the future heavy-ion studies. The ω invariant yields are consistent with the previous publications. The dN/dy for ϕ and J/ψ are 0.010 ± 0.002 (stat.) ± 0.002 (syst.) and $(2.1 \pm$

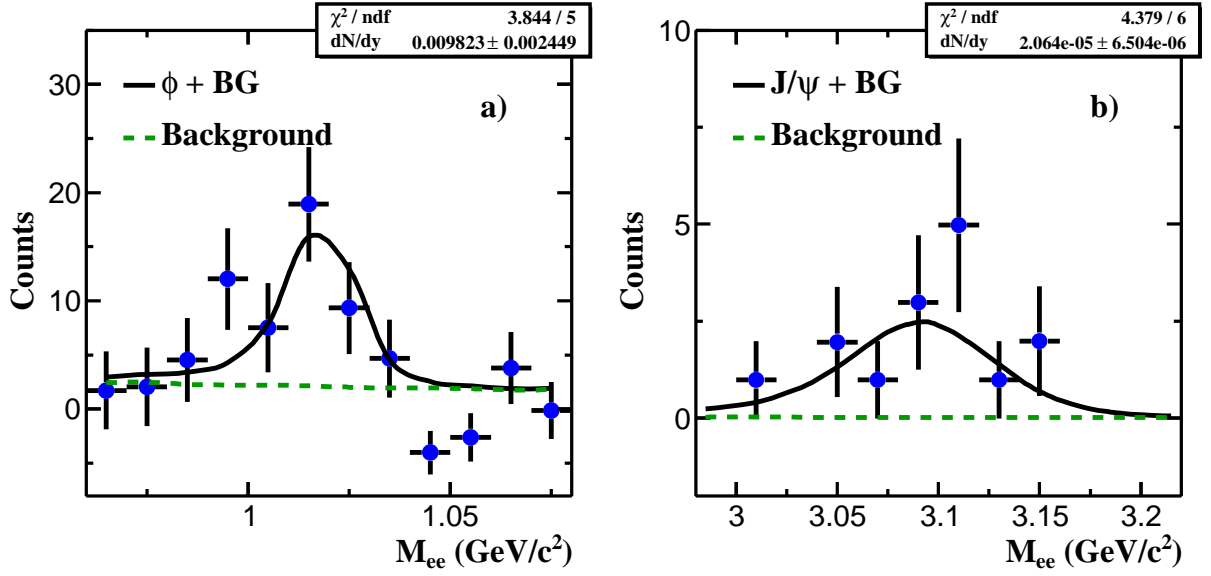


FIG. 16: (Color online) Panel (a): The M_{ee} distribution after the mixed-event background subtraction at $0.95 < M_{ee} < 1.08$ GeV/c^2 in $p+p$ collisions at $\sqrt{s} = 200$ GeV. The curve represents the fit in the range of $0.98 < M_{ee} < 1.04$ GeV/c^2 . Errors on data points are statistical. Panel (b): The M_{ee} distribution after the mixed-event background subtraction at $2.85 < M_{ee} < 3.30$ GeV/c^2 in $p+p$ collisions at $\sqrt{s} = 200$ GeV. The curve represents the fit in the range of $3 < M_{ee} < 3.16$ GeV/c^2 . There is no count in the unlike-sign and like-sign electron-pair distributions at $3.02 < M_{ee} < 3.04$ GeV/c^2 due to statistical fluctuations. Errors on data points are statistical.

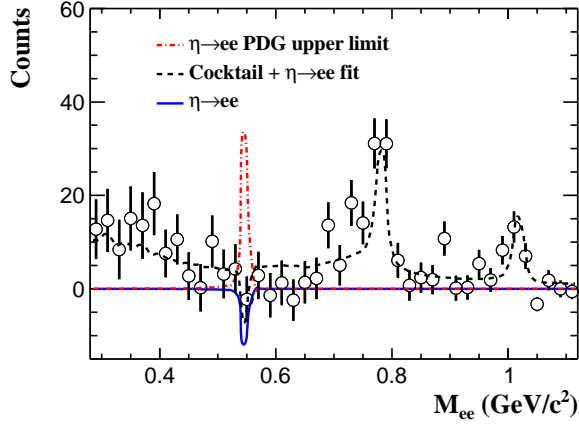


FIG. 17: (Color online) M_{ee} distribution for di-electron production in $p+p$ collisions at $\sqrt{s} = 200$ GeV. The dashed curve is the cocktail with the $\eta \rightarrow e^+e^-$ decay channel included in the fit. The $\eta \rightarrow e^+e^-$ contribution is shown as the solid curve. The dot-dashed peak is the $\eta \rightarrow e^+e^-$ contribution with the upper limit of its branching ratio from the PDG [52], which is 2.7×10^{-5} .

0.7 (stat.) ± 0.7 (syst.) $\times 10^{-5}$, respectively. These results are consistent with the previous measurements from $\phi \rightarrow K^+K^-$ and $J/\psi \rightarrow e^+e^-$. Our measurement lowers the current world limit of the branching ratio of the $\eta \rightarrow e^+e^-$ from 2.7×10^{-5} to 1.7×10^{-5} .

[1] J. Adams *et al.*, Nucl. Phys. A **757**, 102 (2005).
 [2] I. Arsene *et al.*, Nucl. Phys. A **757**, 1 (2005); K. Adcox *et al.*, Nucl. Phys. A **757**, 184 (2005); B.B. Back *et al.*,

Nucl. Phys. A **757**, 28 (2005).
 [3] R. Rapp and J. Wambach, Adv. Nucl. Phys. **25**, 1 (2000).
 [4] G. David, R. Rapp and Z. Xu, Phys. Rept. **462**, 176

- (2008).
- [5] G. Agakichiev *et al.*, Eur. Phys. J. C **41**, 475 (2005).
- [6] R. Arnaldi *et al.*, Phys. Rev. Lett. **96**, 162302 (2006).
- [7] R. Rapp and J. Wambach, Eur. Phys. J. A **6**, 415 (1999).
- [8] G.E. Brown and M. Rho, Phys. Rep. **269**, 333 (1996).
- [9] A. Adare *et al.*, Phys. Rev. C **81**, 034911 (2010).
- [10] A. Adare *et al.*, Phys. Rev. Lett. **104**, 132301 (2010).
- [11] R. Rapp, J. Wambach, and H. van Hees, arXiv:0901.3289; H. van Hees and R. Rapp, Nucl. Phys. A **806**, 339 (2008).
- [12] T. Matsui and H. Satz, Phys. Lett. B **178**, 416 (1986); H. Satz, J. Phys. G **32**, R25 (2006); A. Mocsy and P. Petreczky, Phys. Rev. Lett. **99**, 211602 (2007); Y. Burnier, M. Laine and M. Vepsalainen, JHEP **01**, 043 (2008).
- [13] A.E. Dorokhov, Phys. Part. Nucl. Lett. **7**, 229 (2010).
- [14] J.D. Bjorken *et al.*, Phys. Rev. D **80**, 075018 (2009).
- [15] M.J. Savage, M.E. Luke and M.B. Wise, Phys. Lett. B **291**, 481 (1992).
- [16] L. Bergstrom, Z. Phys. C **14**, 129 (1982); L. Bergstrom *et al.*, Z. Phys. C **37**, 281 (1988).
- [17] L.G. Landsberg, Phys. Rept. **128**, 301 (1985).
- [18] B. Bonner *et al.*, Nucl. Instr. Meth. A **508**, 181 (2003); M. Shao *et al.*, Nucl. Instr. Meth. A **492**, 344 (2002); J. Wu *et al.*, Nucl. Instr. Meth. A **538**, 243 (2005).
- [19] J.M. Landgraf *et al.*, Nucl. Instr. Meth. A **499**, 762 (2003).
- [20] K. H. Ackermann *et al.*, Nucl. Instr. Meth. A **499**, 624 (2003).
- [21] M. Anderson *et al.*, Nucl. Instr. Meth. A **499**, 659 (2003).
- [22] H. Bichsel, Nucl. Instr. Meth. A **562**, 154 (2006).
- [23] Y. Xu *et al.*, Nucl. Instr. Meth. A **614**, 28 (2010).
- [24] M. Shao *et al.*, Nucl. Instr. Meth. A **558**, 419 (2006).
- [25] J. Adams *et al.*, Phys. Lett. B **616**, 8 (2005); L. Ruan, Ph. D. thesis, USTC, 2005, nucl-ex/0503018.
- [26] W.J. Llope *et al.*, Nucl. Instr. Meth. A **522**, 252 (2004).
- [27] J. Adams *et al.*, Phys. Rev. Lett. **91**, 172302 (2003).
- [28] B.I. Abelev *et al.*, Phys. Rev. C **79**, 034909 (2009).
- [29] J. Adams *et al.*, Phys. Rev. Lett. **94**, 062301 (2005).
- [30] L. Ruan *et al.*, Nucl. Phys. A **855**, 269 (2011); B. Huang, Ph. D. thesis, USTC, 2011.
- [31] Z. Tang *et al.*, Phys. Rev. C **79**, 051901 (2009); M. Shao *et al.*, J. Phys. G **37**, 085104 (2010).
- [32] C. Adler *et al.*, Phys. Rev. Lett. **87**, 262302 (2001); J. Adams *et al.*, Phys. Rev. Lett. **92**, 112301 (2004).
- [33] N. M. Kroll and W. Wada, Phys. Rept. **98**, 1355 (1955).
- [34] R. Rapp, Nucl. Phys. A **725**, 254 (2003); E. V. Shuryak and G.E. Brown, Nucl. Phys. A **717**, 322 (2003); P.F. Kolb and M. Prakash, Phys. Rev. C **67**, 044902 (2003).
- [35] J. Adams *et al.*, Phys. Rev. Lett. **92**, 092301 (2004).
- [36] K Nakamura *et al.*, J. Phys. G **37**, 075021 (2010).
- [37] R. Arnaldi *et al.*, Phys. Lett. B **677**, 260 (2009).
- [38] M.N. Achasov *et al.*, Phys. Lett. B **504**, 275 (2001).
- [39] The branching ratio (B.R.) of $\eta' \rightarrow \gamma e^+ e^-$ 4.7×10^{-4} is determined by B.R. of $\eta' \rightarrow \gamma \gamma$ and the ratio of B.R. of $\eta' \rightarrow \gamma e^+ e^-$ to B.R. of $\eta' \rightarrow \gamma \gamma$ [17].
- [40] H. Alvensleben *et al.*, Nucl. Phys. B **25**, 333 (1971).
- [41] J. Adams *et al.*, Phys. Lett. B **637**, 161 (2006).
- [42] J. Adams *et al.*, Phys. Lett. B **612**, 181 (2005).
- [43] S.S. Adler *et al.*, Phys. Rev. C **75**, 024909 (2007).
- [44] S.S. Adler *et al.*, Phys. Rev. C **75**, 051902 (2007).
- [45] A. Adare *et al.*, Phys. Rev. Lett. **98**, 232002 (2007).
- [46] H. Agakishiev *et al.*, Phys. Rev. D **83**, 052006 (2011).
- [47] T. Sjöstrand *et al.*, Comput. Phys. Commun. **135**, 238 (2001).
- [48] A. Adare *et al.*, Phys. Rev. Lett. **97**, 252002 (2006).
- [49] A. Adare *et al.*, Phys. Rev. D **83**, 052004 (2011).
- [50] A. Adare *et al.*, Phys. Rev. C **83**, 024909 (2011).
- [51] B.I. Abelev *et al.*, Phys. Rev. C **80**, 041902 (2009).
- [52] T.E. Browder *et al.*, Phys. Rev. D **56**, 5359 (1997); M. Berlowski *et al.*, Phys. Rev. D **77**, 032004 (2008).